Nuclear Engineering and Technology 51 (2019) 1970–1977

Contents lists available at ScienceDirect

Nuclear Engineering and Technology

journal homepage: www.elsevier.com/locate/net

Original Article

Simulation of the irradiation effect on hardness of Chinese HTGR A508-3 steels with CPFEM

Junfeng Nie*, Pandong Lin, Yunpeng Liu, Haiquan Zhang, Xin Wang

Institute of Nuclear and New Energy Technology, Collaborative Innovation Center of Advanced Nuclear Energy Technology, Key Laboratory of Advanced Reactor Engineering and Safety of Ministry of Education, Tsinghua University, Beijing, 100084, PR China

ARTICLE INFO

Article history:
Received 24 February 2019
Received in revised form
14 June 2019
Accepted 16 June 2019
Available online 19 June 2019

Keywords:
Crystal plasticity
Nano-indentation
Hardness
Irradiation hardening
Ion irradiation

ABSTRACT

Understanding the irradiation hardening effect of structural steels under various irradiation conditions plays an important role in developing advanced nuclear systems. Such being the case, a crystal plasticity model for body-centered cubic (BCC) crystal based on the density of dislocations and irradiation defects is summarized and numerically implemented in this paper. Based on this model, nano-indentation hardness of Chinese A508-3 steels with ion irradiation is calculated. Very good agreement is observed between simulation and experimental data of several different irradiation doses subjected to various operating temperatures, from which, it can be concluded that indentation hardness increases with increasing irradiation dose at both room temperature and high temperature. Consequently, the validity of this model has been proved properly, and furthermore, the model established in this paper could guide the study of irradiation hardening effect and temperature effect to some extent.

1. Introduction

With excellent safety and good economy performance, high-temperature gas-cooled reactors (HTGRs) are recognized as one of reactors for the fourth generation of nuclear power system by the international nuclear community [1]. The reactor pressure vessel (RPV) is a critical and non-replacement component of HTGRs, which plays an important role in sealing radioactive fuel and maintaining operating pressure during the life cycle. However, RPV serves in the hard environment of high temperature, high pressure and adequate irradiation during the operation of HTGR. Therefore, it is very important to choose RPV material with excellent mechanical properties, and the A-5083 steel is selected as the RPV material of the Chinese HTGR. As well known, the lattice atoms of RPV steel become dislocated atoms after being struck by high-energy neutrons and ions, and the irradiation defects are generated through the cascade collision process such as dislocation loops, vacancies, solute clusters, and voids [2,3]. The macroscopic mechanical properties of materials containing irradiation hardening and embrittlement are affected by these irradiation effects.

The irradiation effect is generally studied by ion implantation [4–6], from which, the irradiation condition of ion accelerator can be controlled precisely, the irradiation time required by ion irradiation experiment is short and the cost is low. In the irradiation damage research, nano-indentation method is [7] used to study the mechanical properties of the material for the reason that the irradiation damage caused by ion beam in the material is limited to a few hundred nanometers near the surface.

Weaver et al. [8] used nano-indentation stress-strain curves on unirradiated and proton irradiated 304 stainless steel to quantify the mechanical effects of irradiation damage. They found a significant increase in indentation yield strength and indentation work hardening rate of the irradiated samples. The 315 KeV Ar+9 ions were used to irradiate T-91 steel with the irradiation damage of 5, 10, 20dpa at room temperature by Kumar et al. [9]. The precipitation dissolution phenomenon caused by irradiation was found and the indentation hardness had a saturation as a function of the irradiation dose. Xiazi Xiao et al. [10] developed a mechanistic model for modeling the depth-dependent hardness in ion-irradiated metallic materials. Beyond that, this model could simulate the indentation size effect, ion irradiation induced damage gradient effect, and the soft substrate effect at unirradiated region and the simulation results showed great agreement with the experimental data of several different stainless steels.

It demonstrates that the macroscopic irradiation mechanical properties of the materials are closely relevant to the

* Corresponding author.
E-mail address: niejf@tsinghua.edu.cn (J. Nie).

https://doi.org/10.1016/j.net.2019.06.015

microstructure defects and the irradiation-induced effect is a multi-scale problem. Metal crystal plasticity theory [11] is an important theory that connects mesoscopic scale and macroscopic scale and reveals the deformation law of crystal materials. In addition, irradiation mechanical behavior of crystal materials can be studied from the microscopic view by combining the crystal plasticity theory with the finite element method [12,13].

Although the irradiation hardening effect has been widely investigated, there are few theoretical and numerical studies on the mechanical properties of A5803 steel used in Chinese HTGR under irradiation and non-irradiation, and especially few work is undertaken for the simulations of mechanical properties with CPFEM (crystal plasticity finite element model) from the microscopic view. Such being the case, the work is conducted to simulate the nano-indentation test with CPFEM and understand the fundamental mechanism of the hardness under irradiation. Furthermore, the work is an effective approach to study the irradiation effect at the microscale and predict the mechanical properties to some extent.

In this paper, a body-centered cubic (BCC) crystal plasticity irradiation constitutive model based on the density of dislocation and irradiation defects is implemented. Based on the model, the nano-indentation of Chinese A508-3 steel with different doses at room temperature and high temperature ($250^{\circ}C$) are simulated and the irradiation hardening behavior is studied properly.

2. Crystal plasticity constitutive model coupling with irradiation effect

2.1. Crystal plastic geometry deformation

Crystal plasticity theory is an effective method to study the mechanical behavior of materials at microscopic scale. The deformation of a single crystal is assumed to include the elastic deformation process and the plastic deformation process independently. The deformation gradient $\boldsymbol{F}$ can be decomposed into $\boldsymbol{F^*}$ and $\boldsymbol{F^P}$:

$$\boldsymbol{F} = \boldsymbol{F}^* \cdot \boldsymbol{F^P} \tag{1}$$

where $\boldsymbol{F}^*$ denotes the stretching and rotation of the lattice and $\boldsymbol{F^P}$ is related to crystallographic slip.

Firstly, the crystal translates from the original reference configuration to the intermediate configuration via dislocation slip; then the crystal undergoes lattice distortion and torsion and reaches the current configuration. The mathematical descriptions of crystal plastic deformation and kinematics were derived rigorously by Taylor [14], Asaro [15], Hill and Rice [16].

2.2. Constitutive relation

Following the elastic constitutive relation proposed by Hill and Rice [16], the relation describing the distortion and torsion is given by

$$\overset{\nabla}{\boldsymbol{\sigma}}_{\boldsymbol{Ki}} = \boldsymbol{C} : \boldsymbol{D} - \sum_{\alpha=1}^{n} [\boldsymbol{C} : \boldsymbol{\mu}^{\alpha} + \boldsymbol{\omega}^{\alpha} \cdot \boldsymbol{\sigma}_{\boldsymbol{Ki}} - \boldsymbol{\sigma}_{\boldsymbol{Ki}} \cdot \boldsymbol{\omega}^{\alpha}] \dot{\gamma}^{\alpha} \tag{2}$$

where $\overset{\nabla}{\boldsymbol{\sigma}}_{\boldsymbol{Ki}}$ is the Jaumann derivative of the Kirchoff stress tensor $\boldsymbol{\sigma}_{\boldsymbol{Ki}}$ intermediate configuration, $\boldsymbol{C}$ represents the stiffness tensor, $\boldsymbol{D}$ is the deformation rate tensor, $\boldsymbol{\omega}$ and $\boldsymbol{\mu}$ are the symmetric and anti-symmetric parts of the Schmid factor respectively. The superscript α denotes the considered slip system.

2.3. Flow laws

In the single crystal, slip plays a major role in the plastic deformation. Slip usually occurs in a specific crystal orientation and crystal plane. The specific crystal orientation and crystal plane are called slip direction and slip surface respectively, and the slip surface and slip direction on the surface together are named the slip system. The slip system of crystal is activated when the resolved shear stress on a potential slip plane exceeds its corresponding slip resistance. Furthermore, 48 slip systems are found in BCC crystal.

In the constitutive relation, the slipping rate is critical for the computation. According to Orowan's formula [17], the slipping rate of slip system $\dot{\gamma}^{\alpha}$ is the product of mobile dislocation density ρ_m^{α}, the norm of the Burgers vector b and the mean velocity of the slipping dislocation $\bar{v}^{\alpha}$ and given by

$$\dot{\gamma}^{\alpha} = \rho_m^{\alpha} b \bar{v}^{\alpha} \tag{3}$$

The crystalline slip is assumed to obey Schmid law [18], so the slipping rate $\dot{\gamma}^{\alpha}$ is relevant to the resolved shear stress τ^{α}. For finite deformation, Schmid resolved shear stress is

$$\tau^{\alpha} = \boldsymbol{\sigma}_{\boldsymbol{Ki}} : \boldsymbol{\mu}^{\alpha} \tag{4}$$

When the resolved shear stress τ^{α} exceeds the slip resistance g^{α}, the dislocation starts to slip along the slip direction. The slip in a crystal is thermal-activated. Kothari and Anand [19] proposed the velocity of the slipping dislocation in a Kocks-type activation form [20]:

$$\begin{cases} v^{\alpha} = 0 & \text{if } |\tau^{\alpha}| < g^{\alpha} \\ v^{\alpha} = \bar{l}^{\alpha} v \exp\left\{ -\dfrac{Q_0}{kT}\left[1 - \left(\dfrac{|\tau^{\alpha}| - g^{\alpha}}{\hat{\tau}^{\alpha}}\right)^{p}\right]^{q} \right\} \operatorname{sgn}(\tau^{\alpha}) & \text{if } |\tau^{\alpha}| > g^{\alpha} \end{cases} \tag{5}$$

where $\bar{l}^{\alpha}$ is the mean length of the leading edge of the mobile dislocation, v denotes the vibration frequency of the dislocation, Q_0 represents the activation free energy for slipping without external force, $\hat{\tau}^{\alpha}$ is the maximum slip resistance to be overcome for the movement of the dislocation without thermal activation energy, p and q are the flow laws related parameters respectively. From equations (3) and (5), the slipping rate $\dot{\gamma}^{\alpha}$ can be obtained.

2.4. Irradiation hardening

There are two main hardening mechanisms of the irradiated materials. One is described that in the process of the plastic deformation, dislocation density is increasing gradually and interaction between dislocations is strengthening resulting in a larger slip resistance. Another is that a large number of irradiation defects appear and impede the movement of the dislocation. The irradiation defects mainly include dislocation loops, defect clusters, solute clusters and other defects.

The model implemented in this paper is based on the dislocation loops. The dislocation loops are considered to be the main defects in BCC crystals and other defects are equivalent to the dislocation loops. According to Taylor's hardening law [21,22], the hardening formula coupling irradiation effect is given:

$$g^{\alpha} = Gb\sqrt{q_{\rho}\sum_{\beta=1}^{N}\left[A^{\alpha\beta}\rho_{dis}^{\beta}\right] + q_i N_i^{\alpha} d_i^{\alpha}} \tag{6}$$

where G denotes the shear module, $A^{\alpha\alpha}$ and $A^{\alpha\beta}$ are self and latent

hardening coefficients respectively and represent the contributions of each slip system to the slip resistance of the current slip system, ρ_{dis}^{β} represents the dislocation density of the βth slip system, N_i^{α} and d_i^{α} denote the density and mean size of the dislocation loops in the αth slip system respectively. Meanwhile not all dislocations and irradiation defects contribute to the hardening of the material [10], so we used the coefficients q_ρ and q_i to adjust the ratio of the effective dislocations and defects. N_i^{α} and d_i^{α} can be calculated by Deo's formula [23].

$$N_i^{\alpha} = A \cdot dpa^{1/2} \tag{7}$$

$$d_i^{\alpha} = B \cdot dpa^{1/2} \tag{8}$$

A and B are material constants and the applicable scope ranges from 0.0001dpa to 10dpa.

In a BCC crystal, the mechanism of the dislocation evolution mainly has the following patterns: the multiplication and annihilation of the mobile dislocation, the mobile dislocation trapped as the immobile dislocation, dynamic recovery of the immobile dislocation caused by thermal activation. The total evolution formula of the dislocation density is given as [24].

$$\dot{\rho}_{dis}^{\alpha} = \left(\frac{k_{mul}}{b}\sqrt{\sum_{\beta}\rho_M^{\beta}} - \frac{2R_c}{b}\rho_M^{\alpha} - k_{dyn}\rho_I^{\alpha}\right)\left|\dot{\gamma}^{\alpha}\right| \tag{9}$$

where k_{mul} denotes the multiplication coefficient of the mobile dislocation, ρ_m and ρ_i are the mobile and immobile dislocation density respectively, R_c is the critical size of the annihilation, k_{dyn} represents the dynamic recovery coefficient of the immobile dislocation.

The dislocation loops are assumed to have the similar multiplication form with the mobile dislocations, then the length of the dislocation fragment is changed into $\sqrt{\sum_{\beta}\rho_M^{\beta} + N_i^{\beta}d_i^{\beta}}$. To adjust the influence of dislocations and dislocation loops on the annihilation, the annihilation formula proposed by Patra [25] is modified

$$\dot{N}_{i,ann}^{\alpha}\, d_i^{\alpha} = \frac{R_i^{\alpha}}{b}\left(N_i^{\alpha}d_i^{\alpha}\right)^{c}\left(\rho_I^{\alpha}\right)^{1-c}\left|\dot{\gamma}^{\alpha}\right| \tag{10}$$

As have been noted above, the BCC crystal plasticity model considering irradiation hardening effect has been implemented. In addition, the numerical implementation of the model is completed and the user-defined material subroutine (UMAT) based on ABAQUS [26] is also developed. The flow chart of the finite element implementation is shown in Fig. 1. Nano-indentation of the Chinese HTGR A508-3 steel samples unirradiated and irradiated by different doses at room temperature and high temperature are simulated.

3. Modeling and parameters selection

Tianci Zhang et al. [4] studied the irradiation effect of Chinese A508-3 RPV steel which was used in HTGR. The irradiation source was 3 MeV Fe-ion whose irradiation damage ranges from 0.1 to 20dpa at room temperature and high temperature. Apart from that, positron annihilation doppler broadening (PADB) and nano-indentation method were used to study the macroscopic and microscopic features of irradiated materials. The size of the experimental samples was $10 \times 10 \times 1mm^3$. More details are in Ref. [4].

Since the depth of nano-indentation is smaller than grain size mentioned in Ref. [27], which indicates that a single crystal model should be adopted in the work. According to Ref. [4], the damage indicated by the number of dpa caused by ions ranges from the surface of incidence up to a depth of 1300 nm, and the maximum damage occurs at a depth of about 900 nm. The distribution of irradiation damage is shown in Fig. 2. Furthermore, a conical-shaped indenter with a 70.3°semi-angle is used since the area function is the same as a Berkovich indenter used in the experiments. During the process of experiments, the interface between the indenter and the specimen is assumed to be frictionless. According to references [28–30], the friction has a negligible effect on the load-displacement curve.

Considering the size of indenter and irradiation damage region, the radius and height of the model are both 0.01 mm and it certainly includes the affected area of nano-indentation. Besides, in the pressing direction, the model is divided into sixteen regions where the width of the first fifteen regions is 100 nm. Different region has different dpa value according to Fig. 2. C3D8 is chosen as the element type. At the same time, the meshes near the indenter needed to be enough refined to guarantee the description of deformation below indenter with sufficient accuracy. The model is shown in Fig. 3. In addition, the displacement of the bottom surface is fixed and the loads are applied on the upper surface.

Totally, the indentation depth is 1000 nm. The load-depth profiles are extracted from the data with appropriate interval and the hardness is calculated in the post-process [31]. The nano-indentation processes of Chinese A508-3 steel samples under unirradiated and irradiated conditions at room temperature and high temperature are simulated respectively. For the convenience of description, the depth-dependent dose will be represented by the corresponding maximum dose in the same experiment irradiation situation.

The hardness H is related to P and A:

$$H = \frac{P}{A} \tag{11}$$

where P denotes the load imposed on specimen by indenter and A is the contact area between specimen and indenter. As for ideal Berkovich indenter,

$$A = 24.56h_c^2 \tag{12}$$

where h_c is the contact depth that can be obtained by the simulation directly.

According to Refs. [32–35] and experimental analysis, the main material parameters are shown in Tables 1–4 respectively.

4. Results and analysis

4.1. The load-indentation depth curves and mises stress contour analysis

The indentation hardness as a function of contact depth is calculated for each of the temperatures and irradiation conditions including the unirradiated references. In terms of single crystal, anisotropy is the basic property. Different loading directions will lead to different hardness values. Consequently, the nano-indentation processes are simulated in loading along five typical directions that are along [001], [110], [111], [112], and [123] direction respectively. A set of indentations with a maximum depth of 1000 nm that contain both loading and unloading processes are performed on the surfaces of samples. The corresponding load-displacement curves are shown in Fig. 4. The tendency is consistent with the result shown in Ref. [36]. As shown in Fig. 4, the loads at same indentation depth along [112], [123] and [111] are larger than those along [110] and [001].

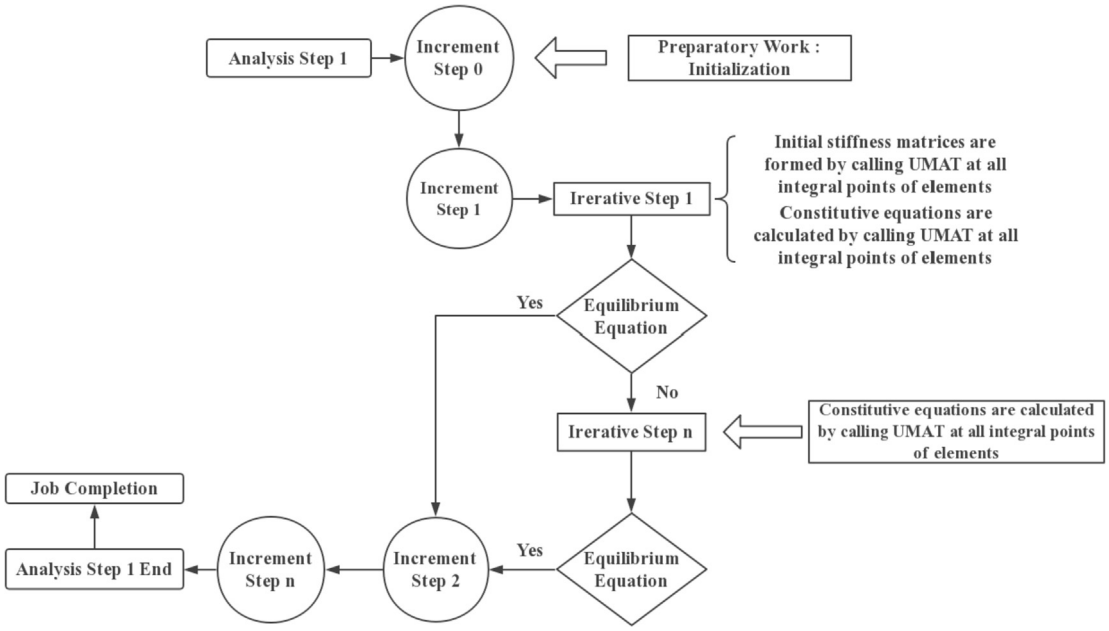

Fig. 1. The flow chart of the finite element implementation.

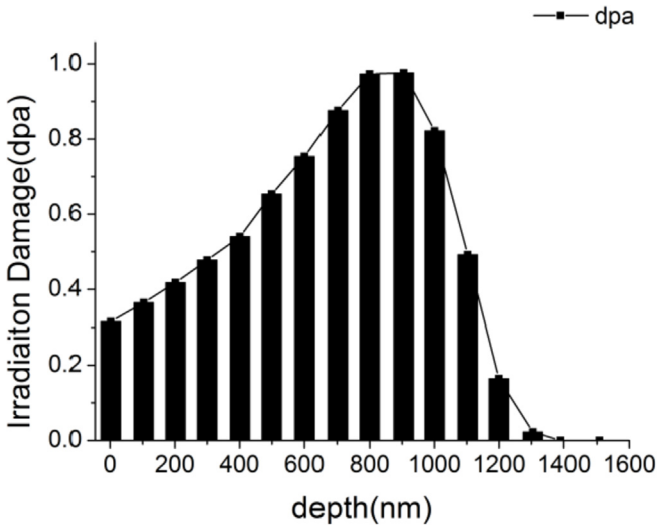

Fig. 2. Depth distribution of damage in the irradiation with a maximum dose of 1dpa calculated by SRIM 2013 [4].

The Mises stress contours of the X-plane at room temperature are shown in Fig. 5. From Fig. 5, non-uniform deformation of the material is observed in [112] and [123]. The indentation hardness of the material is determined by the density of dislocations and irradiation induced defects in the plastic zone. The area of the plastic zone is different along different direction that demonstrates the anisotropy of single crystal. However, they are all basically in the semi-circle area with a radius 7.5 times the indentation depth [10].

Apart from that, the area deeper than 1500 nm is regarded as an unirradiated area and contains little defects, so the hardness of the unirradiated area is smaller. Therefore, when the indentation depth is large and the plastic zone extends to the unirradiated area, the hardness of the nano-indentation measured will be smaller than the hardness measured when the plastic zone is in the irradiated area, resulting in a slow decline of the nano-indentation hardness profiles.

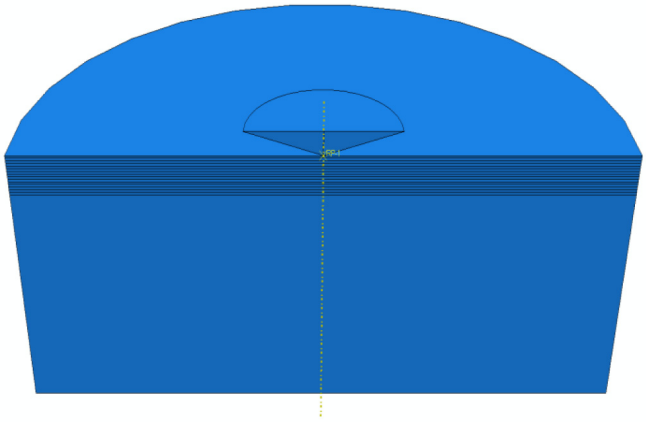

(a) The 16 regions of the model

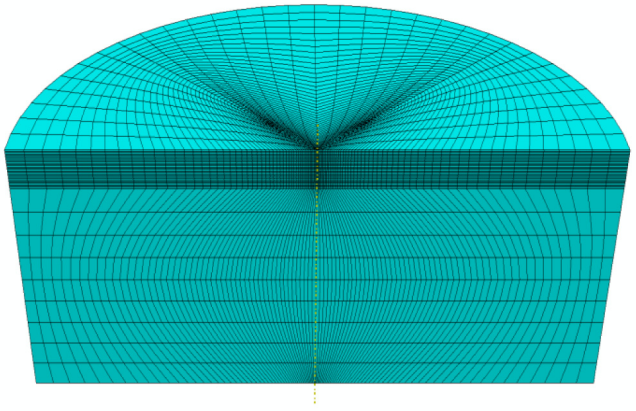

(b) The mesh of the model

Fig. 3. Half of the model in the simulation.

Table 1
The main parameters of elastic module (GPa).

C_{11}	C_{12}	C_{44}
236	134	119

Table 2
The main parameters of flow laws.

$\dot{\gamma}_0$	$\widehat{\tau}_0$	Q_0
$10^7 s^{-1}$	390 MPa	$2.43 \times 10^{-19} J$

Table 3
The main parameters of hardening laws.

k_{mul}	k_{dyn}	β_ρ	q_ρ
0.097	275	0.014	0.06

Table 4
The main parameters of the irradiation effect.

C	β_i	q_i	$A(mm^{-3})$	$B(mm)$
0.98	0.0255	1	5×10^{13}	3.7×10^{-5}

4.2. Nano-indentation hardness analysis

Indentation hardness-depth curves of the simulations at room temperature and high temperature are shown in Fig. 6a-Fig.6c and Fig.7a-Fig. 7c respectively. With given irradiation dose and operating temperature, the values in loading different direction are averaged as final hardness values to decrease the error. Then the final hardness values are compared to the experimental values [4] and shown in Figs. 6d and 7d. First and foremost, the indentation hardness values in loading along [111], [112] and [113] direction are mostly larger than those in loading along [001] and [110]. The phenomenon is also obtained in the load-indentation depth curves. When loading along [112] and [113] direction, it occurs to double slip and [111] is the close packed direction, all of which contributes to the increase of indentation hardness [37]. This result demon-

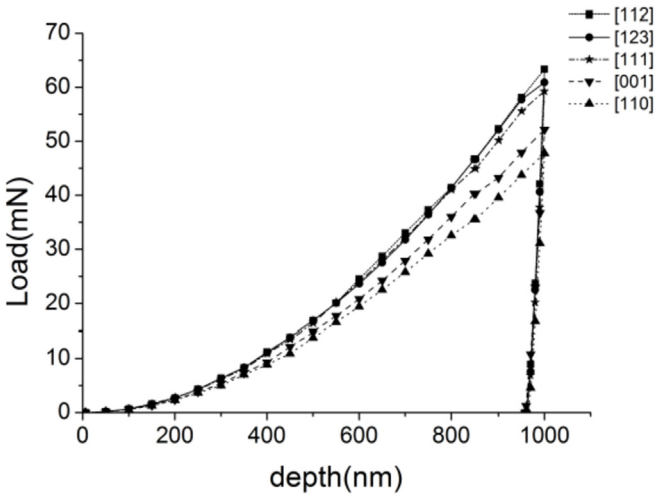

Fig. 4. The load-indentation depth curves under 0dpa at room temperature.

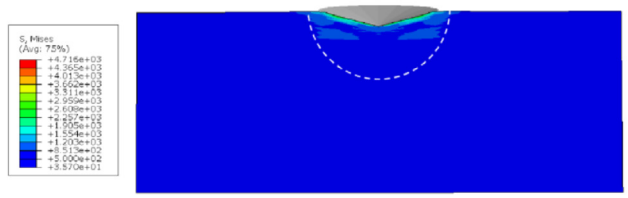

(a) The Mises stress contour in [001]

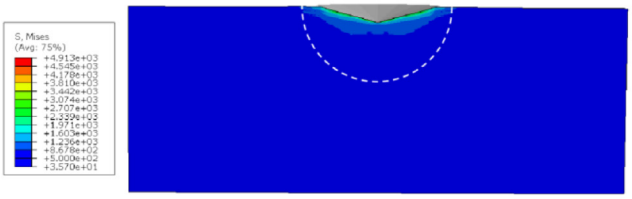

(b) The Mises stress contour in [110]

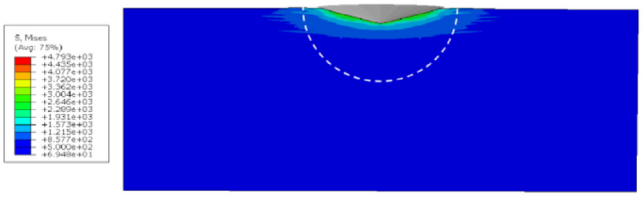

(c) The Mises stress contour in [111]

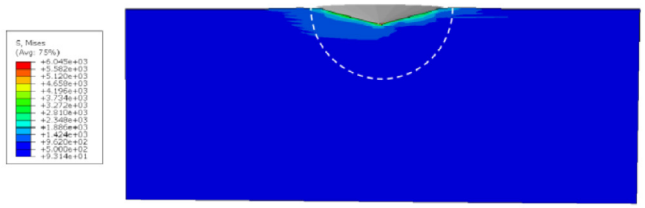

(d) The Mises stress contour in [112]

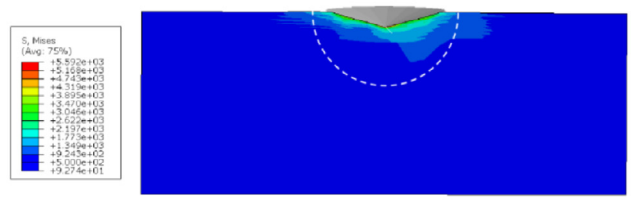

(e) The Mises stress contour in [123]

Fig. 5. The Mises stress contours under 1dpa at room temperature.

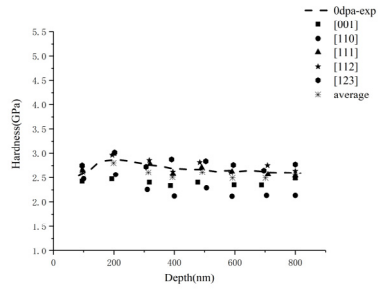

(a) The indentation hardness calculation values in 0 dpa

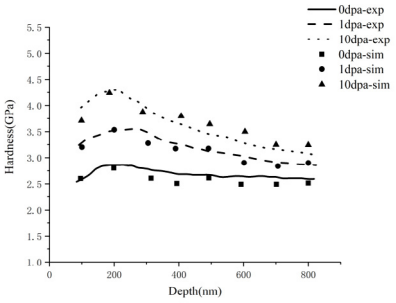

(d) The averaged indentation depth-hardness curves compared to the experimental curves

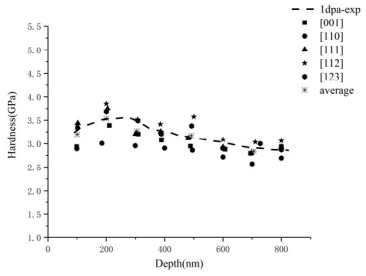

(b) The indentation hardness calculation values in 1 dpa

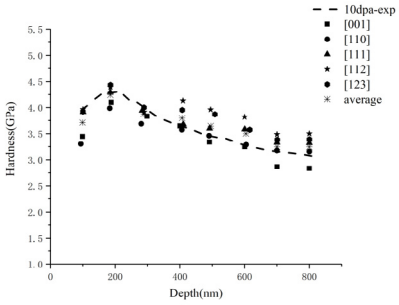

(c) The indentation hardness calculation values in 10 dpa

Fig. 6. The hardness-depth curves of the simulation and experiments with different irradiation damage at room temperature.

strates that the hardness is associated with grain orientation which is evident for our modeling process. From Fig. 6d, it can be obtained that the ion irradiated steel shows an evident hardening phenomenon compared to the unirradiated specimen. The experimental results are the typical hardness-depth profiles in the nano-indentation. The results also show that the hardness increases with the increase of the irradiation dose. Totally, it was associated with the damage defects such as vacancy clusters, dislocation loops, atom clusters and solute clusters. A higher irradiation dose will induce more defects which contribute to the hardness. All the profiles peak at a depth between 150 nm and 250 nm. While across this region, the hardness will decrease with the increase of indentation depth and then descend to stability. Since the change of irradiation defects with depth is taken into account in the model, the numerical simulation results capture the peak characteristics of the hardness and show good agreement with the experimental results. So the validity of the model is proved.

As shown in Fig. 7d, the experimental results show that the tendency of the hardness-depth curves at high temperature is similar to the distribution of hardness along the depth at room temperature, but the hardness of the material irradiated by a high irradiation damage (10dpa) is significantly larger in the area near the surface. In the simulations, temperature effect is considered in the model. These results are in good agreement with the experimental data, especially the simulation results of the unirradiated and 1 dpa irradiated conditions. As for the 10dpa samples, the peak of the hardness calculated by the simulation is smaller than the experimental value. The reason is that the 10dpa samples at high temperature have the higher density of solute clusters and lower density of vacancy-type defects [4], and the formation of solute clusters is thought to be the main reason of the sudden increasing of indentation hardness. In the next study, we will focus on the relationship among irradiation-induced solute clusters, irradiation dose and irradiation temperature to make the model more precise.

5. Conclusion

In this study, a BCC crystal plasticity constitutive model combined with the irradiation hardening effect based on the density of dislocations and irradiation defects is implemented. Using the model, we simulate the nano-indentation of Chinese A508-3 steel samples with ion irradiation in different doses at room temperature

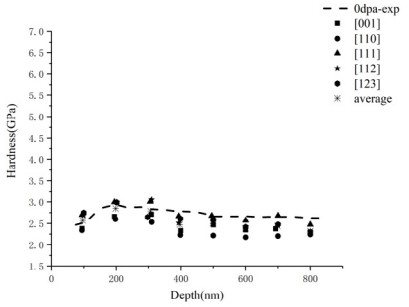

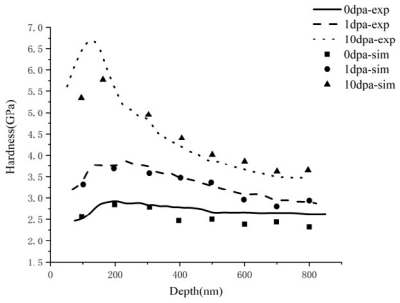

(a) The indentation hardness calculation values in 0 dpa

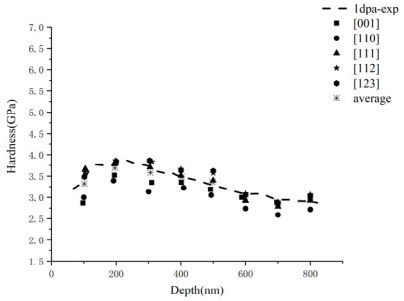

(b) The indentation hardness calculation values in 1dpa

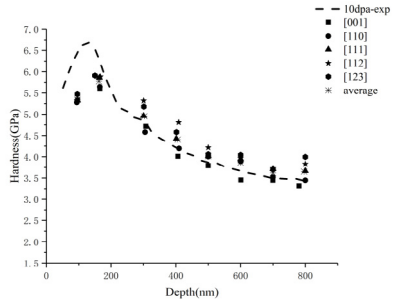

(c) The indentation hardness calculation values in 10dpa

Fig. 7. The hardness-depth curves of the simulation and experiments with different irradiation damage at high temperature.

and high temperature which provides an effective method of studying the irradiation hardening effect. The conclusions have been presented as following:

- The simulations in ion irradiation show good agreement with the experiments, so the validity of the model is proved.
- The model can capture the peaks of the indentation hardness-depth profiles and the hardness of the material increases with the increasing irradiation dose.
- In the results, the temperature effect is also obtained and the connection and tendency between indentation hardness and indentation depth can be also captured.

It also needs to note that the model has not considered the effects of solute cluster defects generated by high dose irradiation at high temperature. Nonetheless, the connection and tendency between indentation hardness and indentation depth can be captured. In a short, it is practicable to study the irradiation effect from a microscopic view using the model, and the model will be improved in the next study.

Acknowledgements

The support of the National Natural Science Foundation of China (NSFC) under Grant No. 11202114, Beijing Higher Education Young Elite Teacher Project under Grant No. YETP0156 and National Science and Technology Major Project of China under Grant No.2017ZX06902012 are gratefully acknowledged.

References

[1] W. Guo, M. Schorer, Development of high temperature gas cooled reactor in China, ATW - Int. J. Nucl. Power 63 (2) (2018) 81.
[2] Z. Jiao, S. Taller, K. Field, G. Yeli, M.P. Moody, G.S. Was, Microstructure evolution of T91 irradiated in the BOR60 fast reactor, J. Nucl. Mater. 504 (2018) 122–134.
[3] Q. Sahi, Y. Kim, Primary radiation damage characterization of alpha-iron under irradiation temperature for various PKA energies, Mater. Res. Express 5 (4) (2018).
[4] T. Zhang, H. Schut, Z. Li, H. Wang, Z. Zhang, M. He, Positron annihilation and nano-indentation analysis of irradiation effects on the microstructure and hardening of A508-3 steels used in Chinese HTGR, J. Nucl. Sci. Technol. 55 (4) (2018) 418–423.
[5] O. El-Atwani, E. Esquivel, M. Efe, E. Aydogan, Y.Q. Wang, E. Martinez, et al.,

Loop and void damage during heavy ion irradiation on nanocrystalline and coarse grained tungsten: microstructure, effect of dpa rate, temperature, and grain size, Acta Mater. 149 (2018) 206–219.
[6] S. Taller, D. Woodley, E. Getto, A.M. Monterrosa, Z. Jiao, O. Toader, et al., Multiple ion beam irradiation for the study of radiation damage in materials, Nucl. Instrum. Methods B 412 (2017) 1–10.
[7] X. Liu, R. Wang, A. Ren, J. Jiang, C. Xu, P. Huang, et al., Evaluation of radiation hardening in ion-irradiated Fe based alloys by nanoindentation, J. Nucl. Mater. 444 (1–3) (2014) 1–6.
[8] J.S. Weaver, S. Pathak, A. Reichardt, H.T. Vo, S.A. Maloy, P. Hosemann, et al., Spherical nanoindentation of proton irradiated 304 stainless steel: a comparison of small scale mechanical test techniques for measuring irradiation hardening, J. Nucl. Mater. 493 (2017) 368–379.
[9] N.N. Kumar, R. Tewari, P. Mukherjee, N. Gayathri, P.V. Durgaprasad, G.S. Taki, et al., Evaluation of Argon ion irradiation hardening of ferritic/martensitic steel-T91 using nanoindentation, X-ray diffraction and TEM techniques, Radiat. Eff. Defect Solid 172 (7–8) (2017) 678–694.
[10] X. Xiao, Q. Chen, H. Yang, H. Duan, J. Qu, A mechanistic model for depth-dependent hardness of ion irradiated metals, J. Nucl. Mater. 485 (2017) 80–89.
[11] A. Kochendoerfer, Theory of crystal plasticity, Z Fur Phys 108 (1938) 244–264.
[12] F.T. Meissornnier, E.P. Busso, N.P. O'Dowd, Finite element implementation of a generalised non-local rate-dependent crystallographic formulation for finite strains, Int. J. Plast. 17 (2001) 601–640.
[13] Junfeng Nie, Yunpeng Liu, Qihao Xie, et al., Study on the irradiation effect of mechanical properties of RPV steels using crystal plasticity model, J. Nucl. Sci. Technol. 51 (2) (2019) 501–509.
[14] G.I. Taylor, Plastic strain in metals, J. Inst. Met. 62 (1928) 307–324.
[15] R.J. Asaro, Micro mechanics of crystals and polycrystals, Adv. Appl. Mech. 23 (8) (1983) 11–15.
[16] R. Hill, J.R. Rice, Constitutive analysis of elastic-plastic crystals at arbitrary strain, J. Mech. Phys. Solids 20 (6) (1972) 401–413.
[17] E. Orowan, Problems of plastic gliding, Proc. Phys. Soc. 52 (1940) 8.
[18] E. Schmid, W. Boas, Plasticity of Crystals. Plasticity and Textures, Springer, Netherlands, 1950.
[19] M. Kothari, L. Anand, Elasto-viscoplastic constitutive equations for polycrystalline metals: application to Tantalum, J. Mech. Phys. Solids 46 (1) (1998) 51–83.
[20] U.F. Kocks, A.S. Argon, M.F. Ashby, Thermodynamics and kinetics of slip, in: B. Chalmers, J.W. Christian, T.B. Massalski (Eds.), Progress in Materials Science, vol. 19, Pergamon Press, Oxford, 1975 p.1.
[21] G.I. Taylor, The mechanism of plastic deformation of crystals. Part I. Theoretical, Proc. Roy. Soc. Lond. 145 (855) (1934) 362–387.
[22] G.I. Taylor, Plastic strain in metals, J. Inst. Met. 62 (1938).
[23] C. Deo, C. Tom, R. Lebensohn, S. Maloy, Modeling and simulation of irradiation hardening in structural ferritic steels for advanced nuclear reactors, J. Nucl. Mater. 377 (1) (2008) 136–140.
[24] J. Nie, Z. Tang, H. Zhang, H. Li, X. Wang, Crystal plasticity constitutive model for BCC based on the dislocation density, Tsinghua Univ(Sci & Technol) 57 (2017) 780–784.
[25] Anirban Patra, David L. McDowell, Crystal plasticity-based constitutive modelling of irradiated bcc structures, Philos. Mag. A 92 (7) (2011) 861–887.
[26] Hibbitt, Karlsson, and Sorensen, ABAQUS, Inc., Providence, RI, v6.5, 2005.
[27] H.E. Xikou, B. Tian, L. Zhengdong, L. Zhaojie, Effect of heating rate and cooling mode on austenite grain size of 508-3 steel, Hot Work. Technol. 42 (20) (2013) 204–205.
[28] A. Bolshakov, G.M. Pharr, Influences of pileup on the measurement of mechanical properties by load and depth sensing indentation techniques, J. Mater. Res. 13 (4) (1998) 10.
[29] K.C. Tang, A. Faulkner, N. Schwarzer, et al., Comparison between an elastic-perfectly plastic finite element model and a purely elastic analytical model for a spherical indenter on a layered substrate[J], Thin Solid Films 300 (1–2) (1997) 177–188.
[30] Y. Wang, D. Raabe, C. Klüber, H. Roters, Orientation dependence of nano-indentation pile-up patterns and of nanoindentation microtextures in copper single crystals, Acta Mater. 52 (8) (2004) 2229–2238.
[31] L. Zhang, Study on Mechanical Properties of Thin Film Nanomechanical Based on ABAQUS Simulation, Jiangsu university, Jiangsu, 2012.
[32] R.A. Johnson, D.J. Oh, Analytic embedded atom method model for BCC metals, J. Mater. Res. 4 (5) (1989) 1195–1201.
[33] S.H. He, B.B. He, K.Y. Zhu, M.X. Huang, Evolution of dislocation density in bainitic steel: modeling and experiments, Acta Mater. 149 (2018) 46–56.
[34] D. Brunner, J. Diehl, Strain-rate and temperature dependence of the tensile flow stress of high-purity α-Iron above 250 K (Regime I) studied by means of stress-relaxation tests, Physica Status Solidi Applied Research 124 (1) (1991) 155–170.
[35] W.A. Spitzig, A.S. Keh, The role of internal and effective stresses in the plastic flow of iron single crystals, Metall. Mater. Trans. B 1 (1970) 3325–3331.
[36] M. Kopernik, A. Milenin, R. Major, J.M. Lakner, Identification of material model of TiN using numerical simulation of nanoindentation test, Metal Science Journal 27 (3) (2011) 604–616.
[37] Jinsheng Pan, Jianmin Tong, Mibo Tian, Materials Science and Engineering, Tsinghua University Press, Beijing, 2010.